

Front tracking velocimetry in advection-reaction-diffusion systems

Thomas D. Nevins^{1,a)} and Douglas H. Kelley^{2,b)}

¹*Department of Physics and Astronomy, University of Rochester, Rochester, New York 14627, USA*

²*Department of Mechanical Engineering, University of Rochester, Rochester, New York 14627, USA*

(Received 19 December 2017; accepted 9 April 2018; published online 27 April 2018)

In advection-reaction-diffusion systems, the spreading of a reactive scalar can be significantly influenced by the flow field in which it grows. In systems with sharp boundaries between reacted and unreacted regions, motion of the reaction fronts that lie at those boundaries can quantify spreading. Here, we present an algorithm for measuring the velocity of reaction fronts in the presence of flow, expanding previous work on tracking reaction fronts without flow. The algorithm provides localized measurements of front speed and can distinguish its two components: one from chemical dynamics and another from the underlying flow. We validate that the algorithm returns the expected front velocity components in two simulations and then show that in complex experimental flows, the measured front velocity maps fronts from one time step to the next self-consistently. Finally, we observe a variation of the chemical speed with flow speed in a variety of experiments with different time scales and length scales. *Published by AIP Publishing.*

<https://doi.org/10.1063/1.5020055>

Many physical systems involve a reactive scalar growing in a fluid flow, including wildfires,¹ combustion,² microfluidic reactors,³ pharmaceutical mixing,⁴ industrial mixers,⁵ and phytoplankton blooms.⁶ Their behaviors can be predicted by knowing reaction front locations and velocities, which depend on advection (fluid flow), molecular diffusion, and reaction (growth). However, since reaction is often nonlinear and the underlying fluid flow can be chaotic or turbulent, complex concentration dynamics are typical in advection-reaction-diffusion (ARD) systems. In previous work,⁷ we showed an algorithm for locating concentration fronts in a reaction-diffusion system and measuring their dynamics. In this paper, we discuss an extension of the algorithm to full ARD systems in two dimensions. The algorithm enables the local measurement of front growth dynamics which allows investigating new questions such as how the growth of reacted regions is affected by fluid flow, how to optimize or control the growth of a reactive scalar, and when ARD simulations can be avoided in favor of simpler front simulations.

been shown to alter front speed through a change in the front shape.^{16–18} In some cases, gentle flow enhances reaction and violent flow inhibits reaction.^{19–21}

By considering a concentration level curve which separates reacted and unreacted regions—a reaction front—the dynamics of ARD, which depend on a partial differential equation (PDE), can be approximated with a simpler dynamics that depends only on ordinary differential equations (ODEs). Burning invariant manifolds (BIMs) and burning Lagrangian Coherent Structures (bLCS), developed from such an approximation, predict when and where a front will advance.^{14,22–27} These theories, along with the commonly used eikonal equation,⁹ rely on the local front velocity being a superposition of the flow velocity and the velocity of a front in a stagnant fluid, which we shall call the “chemical velocity.” In previous work,⁷ we presented an algorithm for measuring the chemical velocity. We tracked growth to obtain velocities and thicknesses (the typical length, across a front, over which the product concentration changes from minimum to maximum) at many locations along fronts. We also showed that velocity and thickness can be used to determine the local diffusivity and reaction rate.

The eikonal approximation and BIM/bLCS theory assume that the chemical velocity of a front is unaffected by flow. By measuring chemical velocity, we hope to test this assumption and determine its limits. Since the ODEs of BIM and bLCS theory are much simpler than the PDE, determining when ODEs are accurate would indicate when full ARD simulations can be avoided in favor of simpler front advection simulations. If ODEs are found to be inaccurate in some flow regimes, front tracking might suggest corrections. For example, the eikonal assumption can include a front curvature correction²⁸ whose magnitude could be measured with front tracking.

Tracking chemical velocity may separately also inform experimental observations of reaction front growth. In recent

I. INTRODUCTION

Adding a flow to the dynamics of reaction-diffusion significantly complicates the motion of reacted regions because the variation of the flow in space and time makes the usual solutions^{8,9} to the reaction-diffusion equation incorrect. With flow, reacted regions grow in different directions and at different speeds from place to place. For instance, frozen fronts are known to persist despite headwinds exceeding the front speed, in contexts including porous media,^{10,11} flow past a bluff body,^{12,13} and vortex flows.^{14,15} Poiseuille flow has

^{a)}Electronic mail: tnevins@ur.rochester.edu

^{b)}Electronic mail: d.h.kelley@rochester.edu

studies of a reaction pinned to a flow obstacle,¹² it was found that the eikonal approximation could explain the selection of frozen fronts but failed to predict the front shape. A deeper understanding of chemical front velocity is needed to understand what caused this difference.

In this paper, we generalize our earlier front tracking algorithm in order to quantify the growth of reacted regions in *flowing* fluid. We put special emphasis on separating the advection of the front from motion of the front relative to the fluid. The algorithm can measure front dynamics in data from experiments or simulations. In the previous literature, the phrase “front tracking” has sometimes referred to a simulation method, where the simulation works differently near a reaction front.^{29,30} Throughout this paper, however, “front tracking” is specifically an algorithm for *measuring* a reaction front in data produced either in simulation or experiment.

We begin our explanation of front tracking with flow in Sec. II, where we will explain how front velocities can be separated into flow velocities and chemical velocities and the physical arguments that justify that separation. In Sec. III, we outline the front tracking algorithm. In Sec. IV, we validate that front tracking provides accurate measurements of total front velocity and chemical front velocity in two simulations: uniform flow and hyperbolic flow. In Sec. V, we describe our experimental apparatus for measuring reaction and flow simultaneously, thereby enabling front tracking with flow in time-dependent ARD experiments. We describe experiments using the excitable Belousov-Zhabotinsky (BZ) reaction in time-independent and time-dependent flows. In Sec. VI, we show the results of front tracking in experiments, demonstrating that front tracking self-consistently maps fronts to the following time step. We also demonstrate the algorithm’s resilience to user parameter choice. Our results suggest a correlation between flow and chemical speed, which we discuss. Finally, in Sec. VII, we describe strengths and weaknesses of the algorithm, opportunities for improvement, and future research questions that may be answered by this algorithm.

II. SEPARATING FLOW VELOCITY FROM CHEMICAL VELOCITY

Our goal in developing this algorithm is to extend the study of reaction front dynamics in ARD systems. Specifically, when a reacted region is subject to simultaneous local reaction, diffusion, and advection by a flow, its edge—the reaction front—moves. Mathematically, the front is a concentration level curve, which moves continuously and according to the ARD equation

$$\frac{\partial c}{\partial t} + (\mathbf{u} \cdot \nabla)c = D\nabla^2 c + F(c). \quad (1)$$

Here, c is a scalar field giving the concentration of the chemical species, \mathbf{u} is the advection velocity, D is the diffusion coefficient of the chemical species in the flowing fluid, and $F(c)$ specifies the reaction kinetics. Because of $F(c)$, the global integral of c typically is not conserved over time. Previously,⁷ we have shown an algorithm for capturing the

front dynamics in a system with $\mathbf{u} = 0$. By measuring the normal displacement of the front at a large number of points, we replicated known front speed,^{8,31,32} and via known solutions to the reaction-diffusion equation,^{8,31,32} we replicated the diffusion coefficient and reaction rate as well.

Here, we present a method for obtaining a front velocity for ARD systems, in which $\mathbf{u} \neq 0$. Advection adds a significant complication because it can move the material in an arbitrary direction. However, the velocity of a front element, \mathbf{w} , can be approximated as

$$\mathbf{w} = \mathbf{u} + \mathbf{v}, \quad (2)$$

where \mathbf{v} is the chemical velocity. The direction of \mathbf{v} is always locally normal to the front because fronts are concentration level curves, and diffusion moves the material down the concentration gradient, normal to the level curves. An example of the result of front tracking, in which \mathbf{u} , \mathbf{v} , and \mathbf{w} have been measured, is shown in Fig. 1. Equation (2), which underlies BIM theory^{14,23} and bLCS theory,²⁶ is drawn from the eikonal approximation. (For a derivation, see Spangler and Edwards.⁹) BIM theory has previously been used successfully to understand front propagation in time independent and periodic flows,^{22,27,33} and the eikonal approximation has proven useful for understanding frozen fronts in adverse flows.^{11,12} Measuring chemical velocity locally could allow quantification of the range of applicability of the eikonal approximation.

III. FRONT TRACKING ALGORITHM

To track fronts, we must first locate them. We begin by finding the edges of the binary field $c > c_{\text{thresh}}$ at a time t , choosing a threshold c_{thresh} that separates reacted regions from unreacted regions. For ARD systems in which characteristic reaction times are much smaller than characteristic diffusion times (that is, the second Damköhler number $Da_{II} = kl_D/D \gg 1$, where $l_D = 1$ mm is a length scale and k is the reaction rate), fronts are sharp, and results are insensitive to the choice of c_{thresh} . For the experiments and simulations discussed below, $Da_{II} = 1300$. Typically, the concentration field c is measured at discrete locations on a grid (pixels), and so, the edges of the binary field $c > c_{\text{thresh}}$ are piecewise-linear curves which follow pixel boundaries and have sharp corners. The true concentration field has no corners because diffusion smooths singularities, and so, we smooth the piecewise-linear curves using a sliding line fit. Smoothing also uses data from adjacent pixels to achieve sub-pixel accuracy in locating the fronts. To correct small-area fluctuating noise in the concentration field, we eliminate $c > c_{\text{thresh}}$ regions that are smaller than a minimum area, which is set by the user. We advise choosing a minimum area that is larger than the data resolution δx but smaller than the smallest structures of interest. We take the smoothed boundaries of the remaining regions to be the original fronts. We repeat the process at a time dt later to locate the subsequent set of fronts, keeping the same value for c_{thresh} . We measure the thickness of both sets of fronts using the same algorithm described previously.²⁰

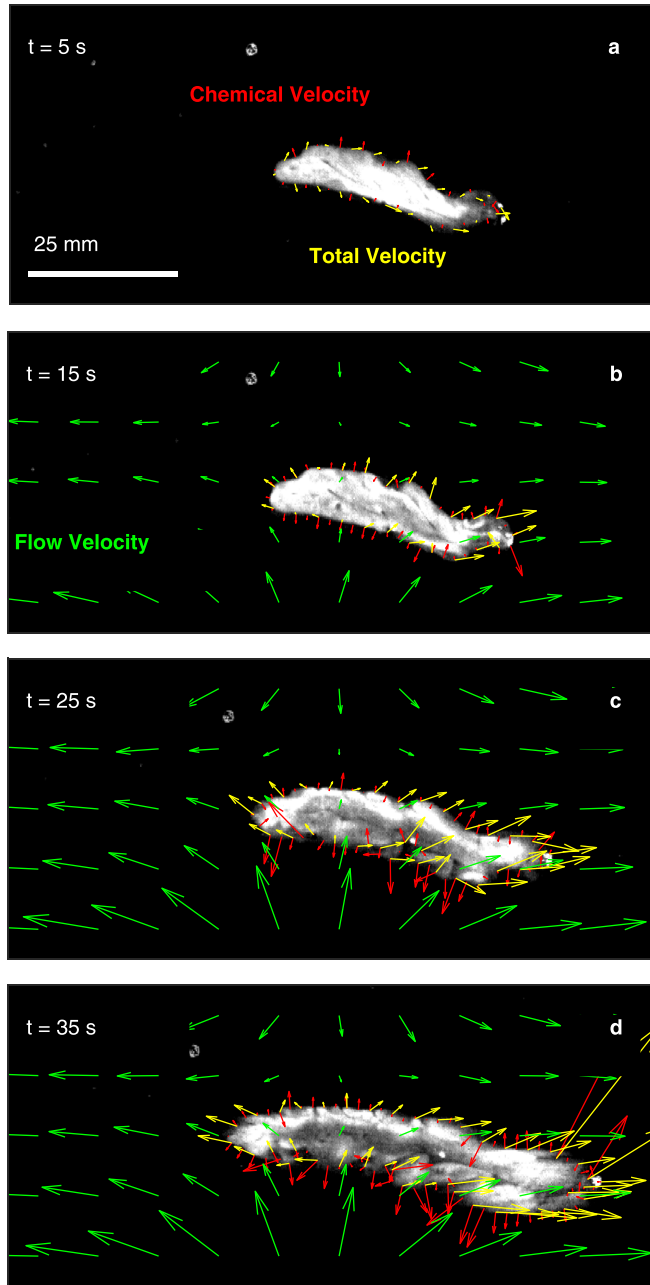


FIG. 1. Example results of front tracking with flow. The product concentration field, measured in an experiment, is shown at four different times. Here and below, shades of gray indicate the product concentration, with the high concentration shown as white and the low concentration shown as black. The measured flow (green), measured total velocity (yellow), and measured chemical velocity (red) are overlaid (and downsampled for readability). Flow was initiated after $t = 5$ s and was fully developed by $t = 25$ s. The chemical velocity is locally normal to the front, and the total velocity depends on flow as well.

The fronts at time $t + dt$ differ from the original fronts at time t by a displacement $d\mathbf{x}_w$ that varies in space and time. Integrating Eq. (2) over time shows that the displacement is due to a combination of flow velocity and chemical velocity

$$d\mathbf{x}_w = d\mathbf{x}_u + d\mathbf{x}_v, \quad (3)$$

where $d\mathbf{x}_u$ is the displacement due to flow and $d\mathbf{x}_v$ is the displacement due to chemical velocity. Assuming that \mathbf{u} is

known, either from simulation or from measurements, then for a fluid element at location \mathbf{x} at time t

$$d\mathbf{x}_u = \int_t^{t+dt} \mathbf{u}(\mathbf{x}) dt', \quad (4)$$

where t' is an integration variable and the integration is performed in a Lagrangian sense, tracking the fluid element as it moves. By integrating all points on the original fronts forward in time according to Eq. (4), we calculate the shapes and positions those fronts would take at time $t + dt$ if they marked high-concentration regions of a passive scalar with zero diffusivity. We refer to the result as the “advected original fronts.”

The displacement between the advected original fronts and the subsequent fronts is $d\mathbf{x}_v$ and can result only from the chemical velocity, which acts in a direction normal to the original fronts, as discussed above. To calculate $d\mathbf{x}_v$ locally, we draw a normal line at a point on the advected original fronts and locate the nearest location where it intersects one of the subsequent fronts; the distance to the intersection is $d\mathbf{x}_v$. We then estimate the local chemical velocity as

$$\mathbf{v} = \frac{d\mathbf{x}_v}{dt}; \quad (5)$$

we emphasize that velocity is approximated by the quotient of the displacement and the time step, both of which are discrete. Finally, we calculate the total displacement $d\mathbf{x}_w$ at each point using Eq. (3) and estimate the total velocity as $\mathbf{w} = d\mathbf{x}_w/dt$. Note that the intersection is unlikely to occur at one of the discrete points identified as being on the subsequent front; intersections typically occur between points. Sometimes, fronts fade or change the shape such that the nearest intersection lies on a different front. To eliminate those non-physical measurements, we discard all displacements larger than a user-defined maximum. Usually, we choose a maximum displacement many times larger than the chemical velocity in stagnant fluid. Figure 2 shows an

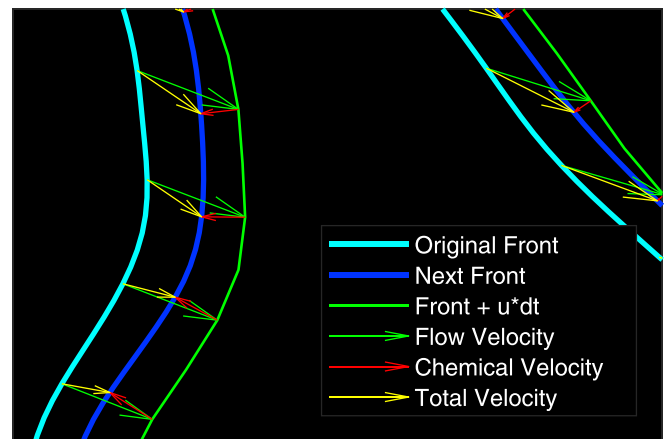


FIG. 2. Cartoon of a single step of front tracking. To determine the displacement due to flow alone, we advect points on the original front by Lagrangian integration of flow data. Where the advected original front differs from the next front (measured one time step later), we attribute the difference to a chemical velocity locally normal to the advected original front. Thus, the total front velocity is the vector sum of flow velocity and chemical velocity.

example in which the original front, advected original front, subsequent front, flow velocity, chemical velocity, and total velocity are all sketched.

We estimate the integral in Eq. (4) using an integration scheme that is first-order in time, and we choose a delay time dt which need not to match the shortest time scale dt_{\min} at which simulation results are calculated or an experiment is imaged. In the results described below, we often choose $dt \neq dt_{\min}$ because $|\mathbf{u}| > |\mathbf{v}|$, such that accurately measuring flow velocity requires a higher frame rate (smaller time step) than measuring chemical velocity. In fact, chemical velocity usually causes fronts to advance only a fraction of a pixel in the time dt_{\min} : $|\mathbf{v}| \ll \delta x/dt_{\min}$, where δx is the size of a pixel (the grid size). Minor noise fluctuations in pixel brightness can therefore appear to cause rapid front motion that is not physical. Choosing $dt > dt_{\min}$ reduces the noise, although dt must be kept small enough that the flow does not alter front perimeters too drastically within a time step. At the same time, choosing dt_{\min} small makes the integration in Eq. (4) more accurate, as we will discuss further below. In our experiments, typically $dt \approx 0.5$ s, while 0.1 s $< dt_{\min} < 0.025$ s.

The algorithm effectively presumes that during each delay time dt , the front advances first by the local flow velocity and then by the local chemical velocity. In reality, both processes act simultaneously. Similar approximations are common in simulations, which often calculate different dynamical terms in sequence. In the limit $dt \rightarrow 0$, the results of the algorithm converge to match the results of both processes acting simultaneously. Still, when dt is finite, advancing the front first by flow velocity and then by chemical velocity introduces small errors to front tracking, due in part to the continuous reorientation of local front elements. The algorithm might also be written to assess the effects of advection and reaction in the opposite order, by advecting the current front *backwards* in time and then attributing the offset between that advected front and the *previous* front to chemical velocity. Evaluating the effects in the opposite order would change the sign of some inaccuracies of numerical integration and differentiation, but the precision would otherwise be similar, and measurements would still converge as $dt \rightarrow 0$.

Written in MATLAB, the open-source algorithm is freely available.³⁴

IV. TRACKING FRONTS IN SIMULATION DATA

We used two series of simulations to test the front tracking algorithm in the presence of flow. First, we performed direct numerical simulations of an ARD system in which the boundary conditions and initial conditions are simple enough that we have clear, *a priori* expectations for the front velocity: a second-order chemical reaction in the presence of a uniform flow. The reaction term is given by

$$F(c) = \alpha c(1 - c), \quad (6)$$

where c is made dimensionless such that it varies between 0 and 1 and α is a scaled reaction rate constant. (We could also write α as kc_0 , where k is the reaction rate in $\text{s}^{-1}\text{M}^{-1}$ and c_0

is the maximum molar concentration, corresponding to $c = 1$.) In the special case of reaction-diffusion ($\mathbf{u} = 0$) in a one-dimensional domain, Eqs. (1) and (6) together become

$$\frac{\partial c}{\partial t} = D \frac{\partial^2 c}{\partial x^2} + \alpha c(1 - c). \quad (7)$$

Equation (7) has an analytic solution^{8,31,32} in which an initial band of high concentration grows in both directions at a constant speed given by

$$v_f = \frac{5}{6} \sqrt{6D\alpha}. \quad (8)$$

In previous work, we showed that front tracking accurately reproduced this front speed in simulation and experiment in the $\mathbf{u} = 0$ case.⁷ Including a uniform flow $\mathbf{u} = U\hat{\mathbf{x}}$ (where U is a constant speed and $\hat{\mathbf{x}}$ is a unit vector in the direction normal to the front) and keeping all other conditions the same, we would expect to observe a propagating band whose edges have fronts with total speeds $w = v_f + U$ and $w = v_f - U$ because the new situation differs from the old one only by a Galilean change in the reference frame.

We simulated Eq. (1) in a two-dimensional periodic domain, using Adams-Bashforth time stepping and central differences for spatial gradients. Initially, the concentration was zero everywhere except in a band where c varied with x according to the analytic solution⁸ of Eq. (7)

$$c(x, 0) = \begin{cases} \frac{1}{(1 + e^{-(x+1)/L})^2} & x \leq 0 \\ \frac{1}{(1 + e^{(x-1)/L})^2} & x > 0, \end{cases} \quad (9)$$

where we define

$$L = \sqrt{6D/\alpha} \quad (10)$$

as the front thickness. The initial concentration did not vary with y , and so, the problem was essentially one-dimensional, consistent with Eq. (8). We chose the values of D and k near those of the Belousov-Zhabotinsky reaction used in the experiments described in Sec. VI. The grid size was $5 \mu\text{m}$, and for stability, we used a $4.11 \mu\text{s}$ time step, saving one concentration field every 0.16 s. We used those concentration fields, along with flow fields $\mathbf{u} = U\hat{\mathbf{x}}$, as inputs for the front tracking algorithm.

Figure 3 shows the results of simulation and subsequent front tracking. In snapshots from one simulation, the reacted region widens and moves to the right as expected. We repeated the simulation first varying the flow speed over the range $0 < U < 2$ mm/s and then varying D to adjust the chemical speed $0.05 \leq v_f < 0.2$ mm/s according to Eq. (8). In all cases, the flow speeds and chemical speeds measured via front tracking closely match the true values. Measurement errors in chemical speed are usually less than $\delta x/dt = 0.03$ mm/s and caused by uncertainty when tracking fronts at sub-pixel accuracy; errors do not grow with true flow speed or with true chemical speed. To confirm, we repeated the tracking, setting dt to be three times as large,

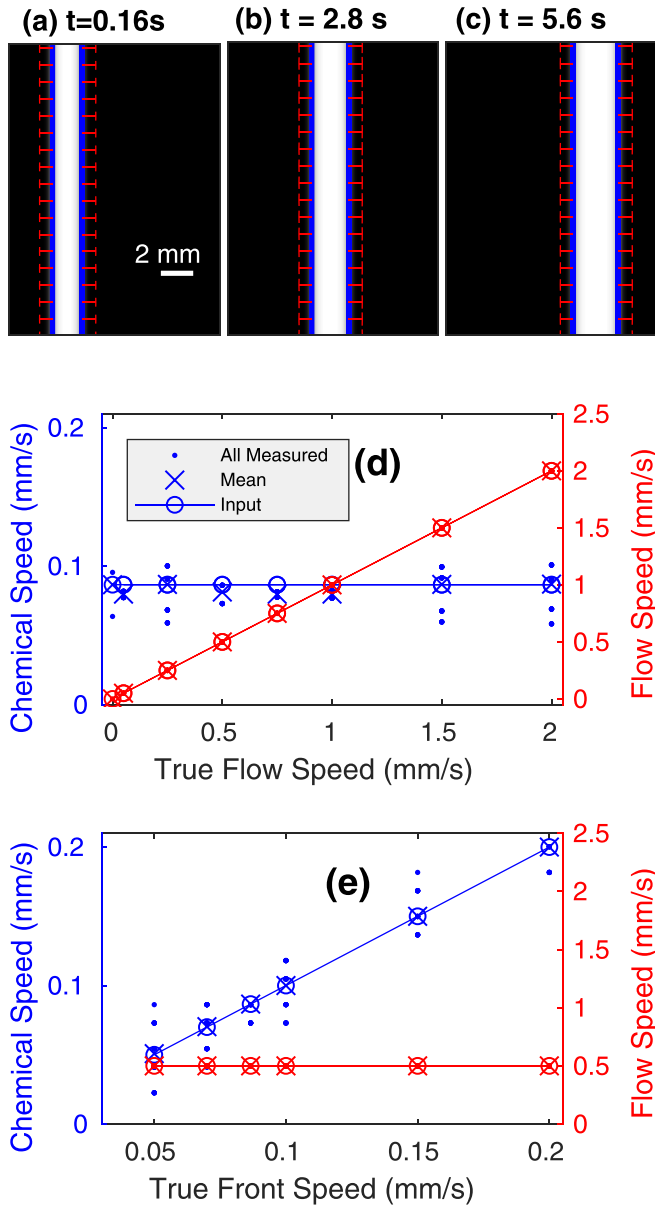


FIG. 3. Validation of front tracking by simulating the advection-reaction-diffusion equations in uniform flow. (a)–(c) Snapshots of a reacted region, showing fronts and chemical velocities determined by the front tracking algorithm. Over time, the front moves to the right and widens. (d) Measurements of the flow speed and chemical speed at the front, for a range of true flow speeds, as simulated. Measurements of chemical speed match true values to within 1 pixel/frame. Dots show all measured chemical speeds at hundreds of locations, although only a few different speeds are observed because of the symmetry of the problem and discreteness of the grid. The mean values also agree closely. (e) Measurements of the flow speed and chemical speed at the front, for a range of true chemical speeds, as simulated. Measured chemical speeds match closely, and measured flow speeds match exactly, as in (d).

and found that the error in chemical speed dropped by a factor of three as expected. Reducing the grid spacing δx would also reduce measurement errors. Although the chemical speed is measured at many locations, only a few distinct values appear in Fig. 3. As mentioned above, the algorithm typically locates fronts with sub-pixel accuracy via spatial smoothing, but in this unusual case of strictly straight fronts, smoothing has no effect, and fronts remain on (discrete)

pixel boundaries, and so, the calculated chemical speeds are discretized.

Considering a one-dimensional front in a uniform flow proved helpful for validating the algorithm because we could form *a priori* expectations of front speed in true advection-reaction-diffusion dynamics governed by Eq. (1). Such a simple case, however, captures no effects caused by complexities in the flow field, such as velocity gradients and front curvature. To further validate the algorithm, we considered another example for which we have *a priori* expectations and in which there are nonzero velocity gradients and curved fronts, although the fronts are no longer governed by Eq. (1). The example is described in Sec. IIIB 1 of the paper by Mitchell and Mahoney:²⁴ a reaction front propagates with constant chemical speed v_0 in potential flow around a hyperbolic critical point at the origin, such that the front dynamics is reduced to a set of ordinary differential equations

$$\begin{aligned} w_x &= \frac{\partial x}{\partial t} = -Ax + v_0 \sin \theta, \\ w_y &= \frac{\partial y}{\partial t} = Ay - v_0 \cos \theta, \\ \frac{\partial \theta}{\partial t} &= 2A \cos \theta \sin \theta. \end{aligned} \quad (11)$$

Here, x and y specify the location of a front element in two dimensions, θ specifies its orientation with respect to the x axis, and A is a positive constant with units of inverse time that sets the speed of the hyperbolic flow. The front dynamics can be calculated from Eq. (11) and are described in a previous paper:²⁴ a front propagating from the left is blocked by a BIM at $x = v_0/A$, while the reacted region continues to spread laterally. Moreover, the dynamics of a front element with orientation $\theta = \pi/2$ can be solved analytically via separation of variables, yielding

$$x = \frac{v_0}{A} + \left(x_0 - \frac{v_0}{A}\right)e^{-At},$$

where x_0 gives one component of the position of the front element at $t = 0$. The front element approaches $x = v_0/A$ at long times, as expected. Front elements with other orientations approach $\theta = \pi/2$ over time because of hyperbolic stretching in the y direction, such that their behavior is asymptotically the same. Differentiating, we find that in the $\theta = \pi/2$ case, the total front speed decays exponentially over time

$$w_x = \frac{\partial x}{\partial t} = -A \left(x_0 - \frac{v_0}{A}\right)e^{-At}. \quad (12)$$

The results of simulating Eq. (11) with $v_0 = 1$ mm/s and $A = 1$ s⁻¹ are shown in Fig. 4. A front that is initially circular and positioned left of the hyperbolic point approaches the BIM and stretches laterally, as expected. Applying the front tracking algorithm, we measure $\langle w_x \rangle$ as it varies in time, finding close agreement with Eq. (12). Measurements of chemical speed v are more complicated and illustrate the balance required in choosing input parameters because of the finite resolution of the data. As Fig. 4 shows, when we

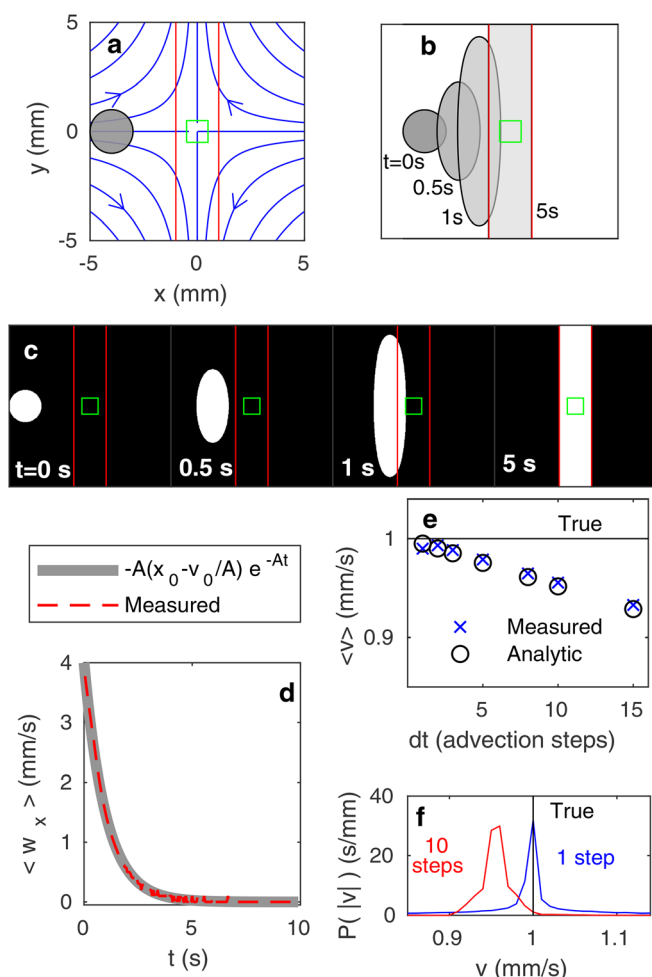


FIG. 4. Validation of front tracking by simulating an advancing front near a hyperbolic critical point. (a) Flow field (blue streamlines), hyperbolic point (green square), BIMs (red lines), and initially reacted region (gray). (b) Simulated front at four subsequent times. (c) Corresponding concentration fields at the same times, constructed from the simulated front. (d) Measured mean total front speed $\langle w_x \rangle$ closely matches Eq. (12), as expected. (e) When dt is small, the distribution of local chemical speeds is peaked very near the true value, but the distribution has long tails. Increasing dt shifts the peak but shortens the tails. (f) Tracked fronts have mean chemical speed $\langle v \rangle$ that closely matches the true value, 1 mm/s, when dt is small but diverges as dt is increased.

choose $dt = dt_{\min}$, the distribution of chemical speed measurements has a sharp peak at 1 mm/s, matching the true value. However, the distribution also has long tails: at some locations, the measured chemical speed differs substantially from the true value. As discussed above, choosing $dt > dt_{\min}$ can reduce noise in the chemical speed measurements. Choosing $dt = 10dt_{\min}$ not only shortens the tails as expected but also moves the peak of the distribution away from the true chemical speed by a few percent. Choosing $dt > dt_{\min}$ also moves the mean value $\langle v \rangle$ away from the true value by a few percent, as shown.

This discrepancy is caused by the nonzero velocity gradient of this flow and by using discrete approximations for derivatives. In this example, most measurements occur near the BIM, where the total front speed is zero, and so, the true chemical velocity is equal and opposite to the true flow velocity [Eq. (2)]. To measure the chemical velocity, the

algorithm first uses Eq. (4) to calculate $d\mathbf{x}_u$, the displacement of the front over time dt by flow alone. Since $d\mathbf{x}_w = 0$ at the BIM, $d\mathbf{x}_v = -d\mathbf{x}_u$, according to Eq. (3). Finally, the algorithm calculates the chemical speed using Eq. (5), which estimates a derivative by simple division. If $dt = dt_{\min}$, then Eq. (4) reduces to $d\mathbf{x}_u = \mathbf{u}(\mathbf{x}) dt$ (an integral estimated by simple multiplication) and the algorithm measures the true chemical speed exactly. Similarly, if the velocity gradient is zero, the velocity remains constant over the integral in Eq. (4), which again yields $d\mathbf{x}_u = \mathbf{u}(\mathbf{x}) dt$, and so, the true chemical speed is again measured exactly. However, if $dt > dt_{\min}$ and the velocity gradient is nonzero, a small systematic error occurs. Estimating the integral in Eq. (4) by summing over multiple steps of size dt_{\min} produces a higher-precision result than Eq. (5), which estimates a derivative with a single step of size dt . This effect can cause front speed measurements to deviate from expectations by a few percent in this example, as shown in Fig. 4.

Setting $dt = dt_{\min}$ eliminates the discrepancy illustrated in Fig. 4 but increases measurement noise caused when the chemical speed is less than $\delta x/dt$, as discussed above. Thus, we leave dt as a user-specified parameter instead of setting $dt = dt_{\min}$ everywhere and allow users to make their own decisions about the trade-off. The best solution is to minimize δx by increasing the spatial resolution of the simulations or experiments to which the front tracking algorithm is applied. Moreover, the simulation shown in Fig. 4 represents an extreme case since the front aligns with the BIM, where this error is maximized. In experiments, we observe much smaller errors, as described in Sec. VI.

V. EXPERIMENTAL ADVECTION-REACTION-DIFFUSION DEVICES

Having verified that the results of tracking fronts in a simple, simulated ARD system closely match our expectations, we set out to track fronts in ARD experiments. Below we show the results from three different devices that drive three different flow patterns but use the same chemistry and imaging apparatus, similar to what we used in previous work.^{7,20} We track fronts produced by the Belousov-Zhabotinsky (BZ) reaction.^{32,35–38} BZ is an excitable redox reaction catalyzed by a ferroin indicator. We prepare BZ using the recipe of Bargteil and Solomon,²² adding ferroin throughout the experiment to maintain contrast. Ferroin is known to have a negligible effect on front speed.³⁶ We initiate reaction at a chosen location by immersing a silver wire for ~ 20 s. A large number of inert $98 \mu\text{m}$ fluorescent green tracer particles (Cospheric UVPMS-BG-1.025) float on the surface of the fluid layer and make its motion visible. These particles are small enough to follow the flow accurately, as indicated by their small Stokes number $St \leq 0.5$.

Experiments are illuminated with blue light-emitting diodes (LEDs), which excite the tracer particles, causing them to fluoresce green. The BZ solution is blue in its reacted state and red in its unreacted state, and so, reacted regions appear brighter. We use a magenta background beneath the fluid layer to produce good contrast with both the blue BZ reacted state and the green tracer particles. We

image BZ experiments with two hardware-synchronized cameras (Emergent HS-4000M), as sketched in Fig. 5. One camera images the concentration field and is equipped with an optical filter that passes blue light but blocks green to accentuate the blue reacted regions while minimizing the visibility of the green tracer particles. The brightness of its images measures the BZ product concentration. The other camera images particle positions and is equipped with an optical filter that passes green light but blocks blue to accentuate particles while minimizing the visibility of the reaction state. Particle tracking³⁹ provides the flow field. Although the cameras are mounted close together, their fields of view are not identical. Before taking data, we photograph a calibration grid with both cameras, which allows us to determine their relative shift and rotation and the resolutions of both. In the experiments described below, resolutions are typically about $150\ \mu\text{m}/\text{pixel}$. Each camera records images that are 2048×2048 pixels. We vary the frame rate depending on the flow speed, sometimes imaging as rapidly as 40 Hz, but more typically imaging around 10 Hz. Together, the two cameras measure the concentration field c and flow field \mathbf{u}

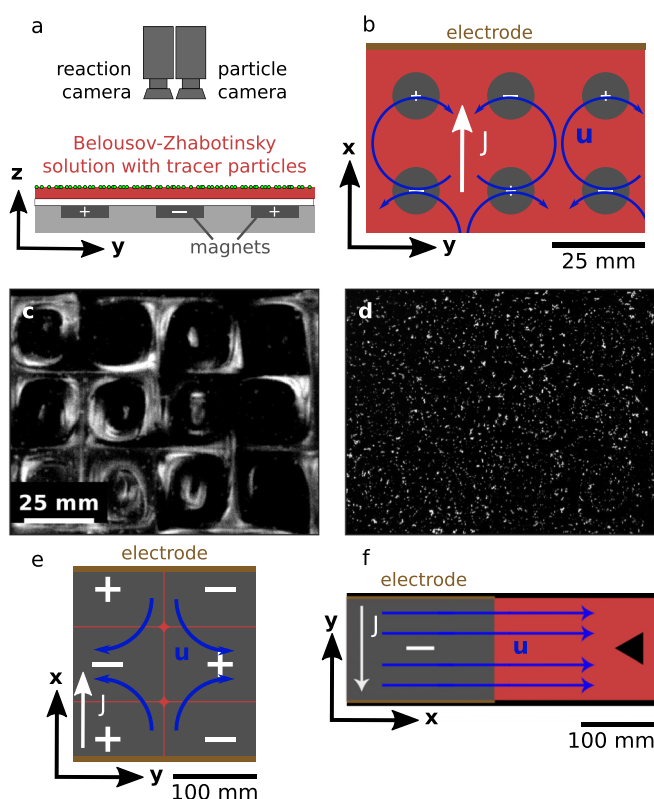


FIG. 5. Laboratory advection-reaction-diffusion devices and typical data. (a) Two hardware-synchronized cameras image a thin layer of BZ solution containing green fluorescent tracer particles. One camera images the product concentration, while the other camera images particles. (b) Flow is driven by an electric current J in the x direction, which interacts with a magnetic field in the z direction. In the small-length-scale vortex flow device, the field is produced by a checkerboard array of small magnets below the fluid that drive vortices. (c) Snapshot of the color of the BZ reaction, used to measure the product concentration. (d) Simultaneous snapshot of tracer particles, used to measure flow. (e) The large-length-scale vortex flow device is similar but uses larger magnets to produce vortices with a larger characteristic length scale. (f) The water channel device uses magnets to drive flow past a bluff body.

throughout space and time, providing the necessary inputs for front tracking.

In all three experimental devices, we drive flow electro-magnetically by passing electrical current through the fluid layer with permanent magnets nearby. Two of the devices are built with magnets whose orientation alternates like a checkerboard and are sketched in Fig. 5. In one, cylindrical NdFeB magnets with diameter 12.7 mm are spaced 25.4 mm on the center, and the vessel has lateral dimensions $254\text{ mm} \times 254\text{ mm}$, producing a 10×10 square array of alternating vortices. In the other, rectangular ceramic magnets with lateral dimensions $152.4\text{ mm} \times 101.6\text{ mm}$ are tiled tightly beneath the same vessel, producing a 2×2 rectangular array with a larger length scale. Both devices produce flows dominated by vorticity (not shear), but the characteristic flow length scales differ substantially. The third device is a water channel that produces a wake behind a bluff body, previously described in detail.²¹ The bluff body is an equilateral triangle with a side length of 45 mm, positioned symmetrically about the channel center with one vertex pointing upstream. The channel flow is dominated by shear (not vorticity) except in the wake behind the bluff body. In all three devices, the depth h is sufficiently small that the flow is quasi-two dimensional, although the front tracking algorithm could be adapted to three-dimensional systems as well.

VI. TRACKING FRONTS IN EXPERIMENTAL DATA

The experimental flows produced by our three ARD devices are more complicated than the flows considered in the simulations described in Sec. IV, and so, forming *a priori* expectations for front velocities is difficult. Nonetheless, we can use experimental measurements to show that the front tracking algorithm is self-consistent. We can also use local measurements of front velocity to explore ARD phenomena beyond the eikonal approximation, such as variation of chemical speed with flow speed.

Figure 6 verifies the self-consistency of the algorithm in four cases, using data from the uniform-flow simulation and from all three experimental devices. In each snapshot, a concentration field is overlaid with the fronts located in that concentration field, the fronts located in the next concentration field, and the result of advecting the original front. Finally, the figure also shows original fronts displaced by $d\mathbf{x}_u + d\mathbf{x}_v$, accounting for both the local flow velocity and the local chemical velocity. According to Eq. (3) and our definition of $d\mathbf{x}_w$, those displaced fronts should exactly match the fronts in the next concentration field. The close agreement shown in Fig. 6 shows that the algorithm is implemented correctly. In practice, the match is not perfect because continuous, curved fronts are approximated by straight lines between discrete points, and the number of points need not remain constant over time. Nonetheless, the close match shows that with sufficient spatial resolution, the error in total velocity is small in four different flows that vary in complexity, length scale, and speed and whether their domain is open (as in the simulation and behind the bluff body) or closed (as in the vortex flows).

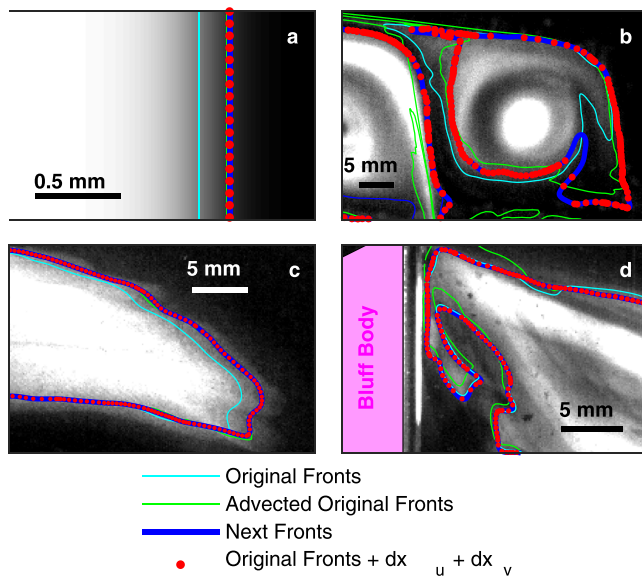


FIG. 6. Front velocity measurements are consistent with measured front locations in simulation and in three different experimental devices. (a) Simulation of uniform flow. (b) Vortex-dominated flow with a small length scale. (c) Vortex-dominated flow with a large length scale. (d) Wake of a bluff body. The original front, displaced by $dx_u + dx_v$, closely matches the next front, indicating that the algorithm is self-consistent and that discretization errors are negligible at the given spatial resolution.

In addition to velocity and concentration fields, the front tracking algorithm requires user-specified parameters. It is important to know whether small variations in those parameters, especially the brightness threshold c_{thresh} and the time step dt , significantly affect the results of front tracking. We repeatedly tracked fronts in the same experiment, varying those two parameters widely, and Fig. 7 shows the results. The change in the median and root-mean-square chemical speed is much smaller than the interquartile range (the range between the 25th and 75th percentile) at many parameter values, indicating that a wide range of c_{thresh} and dt choices provide similar results. Excessively low thresholds cause measured front locations to change suddenly with minor brightness variations, artificially inflating the chemical speed. Excessively high thresholds cause some fronts to go

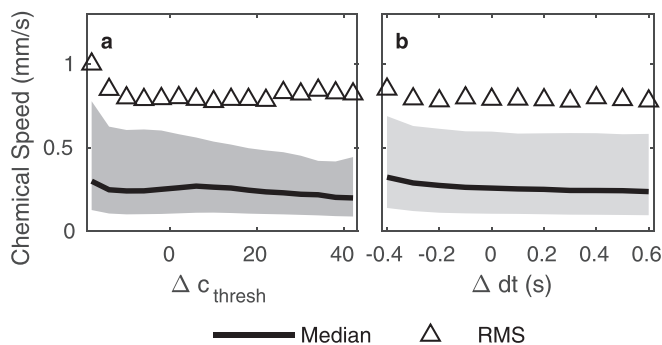


FIG. 7. (a) Variation of statistics of chemical speed with Δc_{thresh} , defined as the difference between the actual threshold and the reference threshold used to produce Fig. 9. The gray region indicates the interquartile range, and the triangles indicate the root-mean-square (RMS) chemical speed. The plot ranges from values as dim as the background to values as bright as the reacted region. (b) Variation of statistics of chemical speed with time step dt . The gray region again indicates the interquartile range.

undetected. Time steps significantly smaller than the typical time required for a front to advance by one pixel introduce noise that artificially inflates the chemical speed. Increasing the spatial resolution allows reducing dt further. Excessively large time steps also reduce accuracy, as described above and shown in Fig. 4.

Because front tracking provides local measurements of flow velocity and chemical velocity, it can make measurements statistically robust. For example, the chemical velocity can be measured at many locations along a front in order to determine its mean and moments with great accuracy when the only likely source of variation is random noise.⁷ Perhaps more interestingly, front tracking can measure the variation of chemical velocity and front thickness in space and time when significant physical mechanisms cause that variation. In Fig. 8, we plot probability density functions for chemical velocity in the x and y directions. To do this, we find front points at the same location and time in a front tracking with dt equal to that in Fig. 9 and dt twice as large. We find that the most likely local front velocity difference is zero, indicating good match between the two locally. Errors caused by choosing $dt > dt_{\text{min}}$, which shifted the peak of the chemical velocity distribution by as much as a few percent in the example of a front propagating through a hyperbolic flow (Sec. IV), are negligible in this experimental example. Differences in v_y are somewhat larger than those in v_x because in this experiment, the front advances primarily in the y direction, resulting in higher average speeds in the y direction.

Having validated the front tracking algorithm in simulation and experiment, and having shown that the algorithm is robust to the variation of input parameters, we measured distributions of chemical speed in both the small-scale and large-scale vortex flows. Figure 9 shows a typical concentration field from each set of experiments. We measured the chemical speed between 8×10^4 and 2×10^6 locations over durations ranging from 36 s to 800 s. In the small-scale device, we varied the flow speed (characterized by the root-mean-square speed u_{rms}) over two orders of magnitude, using a different, constant current for each experiment. We find that the distribution of chemical speed changes with flow

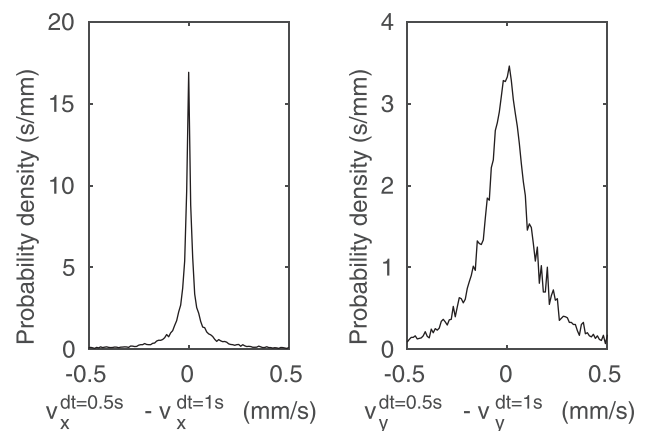


FIG. 8. Distributions of the change in chemical velocity components caused by changing the time step dt from 0.5 s to 1 s. Both distributions are symmetric and peak at zero, indicating a match.

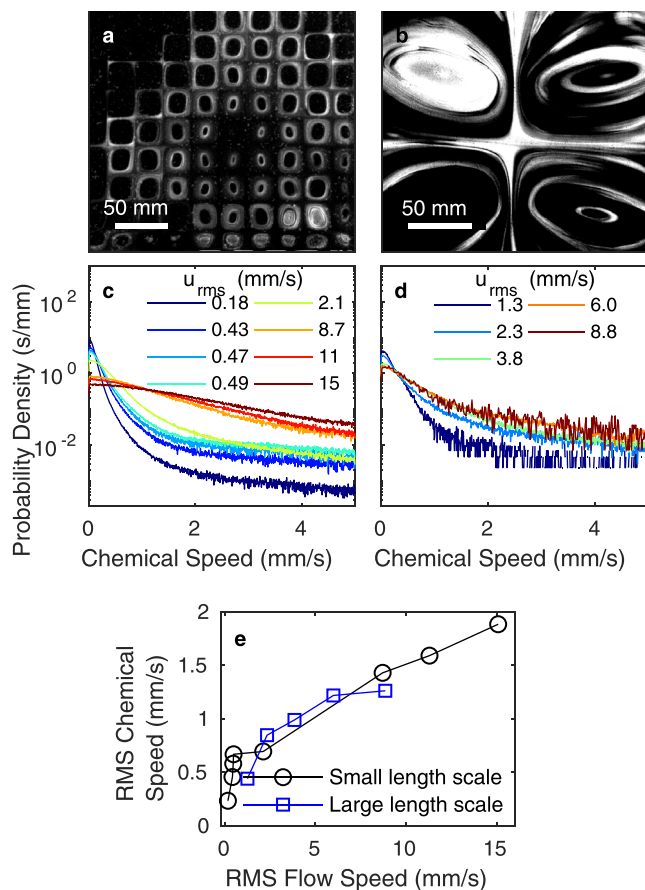


FIG. 9. Concentration fields in vortex-dominated experimental flows with small (a) and large (b) characteristic forcing scales. (c) Distributions of chemical velocity in vortex-dominated flows with small characteristic forcing scale for various root-mean-square (RMS) flow speeds. (d) Distributions of chemical velocity in vortex-dominated flows with a large characteristic forcing scale, for various root-mean-square flow speeds. In both cases, higher flow speeds cause longer probability tails, indicating greater probability of high chemical velocity. (e) Root-mean-square reaction speed increases with root-mean-square flow speed, and measurements from experiments with two different characteristic forcing scales nearly collapse.

speed. The distribution varies nearly monotonically, growing a longer tail, signifying a greater prevalence of high front speeds as u_{rms} increases. In the large-scale device, because the magnets are weaker, we are unable to vary u_{rms} as widely. Still, over a range of flow speeds, we observe the same trend: regions where fronts have high chemical speed become less rare as the flow becomes faster. These results suggest that the basic eikonal approximation, in which chemical speed is constant,⁹ does not capture the full dynamics of these experiments.

Seeing the same trend in experiments using two different devices suggests that a quantitative comparison might provide insights. We reduced each distribution to a single measurement, the root-mean-square chemical speed v_{rms} of all fronts at all locations and times in the experiment. Surprisingly, plotting v_{rms} against u_{rms} for experiments in both the small-scale and large-scale device on the same axes, as in Fig. 9(e), shows that the two curves collapse to show a single trend. Neither scaling nor fit parameters are required for the collapse.

Many mechanisms might explain the observed deviation from the eikonal approximation. The eikonal approximation

requires that the second Damköhler number, the Thiele number, and the first Damköhler number are all large. In these experiments, the second Damköhler number is $Da_{II} = 1300$, and so, we do not expect Da_{II} to explain the variation of chemical speed with flow speed. The Thiele number $\Phi^2 = Da_I Pe$ relates advection, diffusion, and reaction times, where $Pe = UL/D$ and $Da_I = kU/L$ (L is the flow length scale). In these experiments, $\Phi^2 > 7.7 \times 10^5$, and so, we do not expect Φ^2 to explain, either. The first Damköhler number relates the reaction rate to the advection rate. These experiments span the range $2 \leq Da_I \leq 183$, in which $Da_I \gg 1$ is not strictly true, and we expect the small values of Da_I account for some deviation from the eikonal approximation. In fact, we believe the $Da_I \sim 1$ regime to be particularly interesting because neither advection nor reaction can be neglected and because it is likely relevant for modeling marine phytoplankton, whose growth rate nearly matches the tidal time scale. That said, many previous studies have considered the $Da_I \gg 1$ case, and we speculate that chemical speed is nearly uniform in that regime.

Front curvature has also been observed to affect front speed²⁸ and might explain the variation we observe. However, the curvature correction term to the eikonal approximation is proportional not only to curvature but also to diffusivity. Considering the effective diffusivity of BZ products and the typical speed of BZ fronts, the term becomes appreciable only when the curvature exceeds 100 mm^{-1} or, equivalently, when fronts have a radius of curvature less than $10 \mu\text{m}$. Curvature effects cannot explain our observations because the apparatus described in Sec. V cannot resolve such small scales. Moreover, at the scales, we can observe that the vast majority of chemical velocity measurements come from locations where fronts are nearly zero curvature.

Our experiments are meant to approximate two-dimensional flow, but the actual flow varies vertically and drops to zero at the vessel floor, which is a no-slip boundary. Reaction fronts are therefore sheared vertically, which causes three-dimensional concentration variations and corresponding brightness variations that differ from those expected for purely two-dimensional fronts. The differences may account for some of the chemical speed variation we measure. One specific three-dimensional phenomenon that results from the no-slip boundary is Ekman pumping. Ekman pumping is a secondary flow that results from the fact that rotation generates a radial pressure gradient. This pressure gradient persists in the boundary layer, but flow there is too slow to balance the pressure gradient. The result is upwelling at vortex centers and downwelling at vortex edges, both of which cause mixing⁴⁰ and could affect the measured front speed. In our experiments, we sometimes observe high front speed where fronts propagate into vortices, as would be caused by Ekman pumping. However, although we would expect the effects of Ekman pumping to differ in vortices having different sizes (and therefore different angular momenta), we have not observed such differences. Future experiments could include an immiscible lubrication layer between the reacting fluid and the vessel floor to greatly reduce shear and therefore both Ekman pumping and three

dimensional concentration gradients. Shear can also be reduced by using deeper fluid layers. We have performed experiments with varying depths, however, and find no dependence of the chemical speed variation on the depth. Thus, the effect of shear may be small.

We have observed in previous work⁷ that the front and “back” of a BZ reacted region have different properties because the chemical kinetics during the transition from the unreacted to the reacted state (at reaction fronts) differ from those during the return to the unreacted state (at reaction backs). In stagnant fluid, both fronts and backs advance with the same chemical velocity, as required by the fixed refractory time that separates them. However, fronts and backs have different thicknesses, one indication that they may be affected differently by an underlying flow. However, examination of a single front with no back in Fig. 7 still showed a wide chemical speed distribution and summary statistics much faster than the speed of BZ fronts in stagnant fluid. We hope to track fronts and backs separately in future work to test the extent to which the difference in their chemical kinetics explains the variation of chemical speed with flow speed.

The stretching and collision of fronts might also increase front speeds. One recent study found behavior consistent with the chemical speed of BZ fronts being unaffected by flow²² but rarely measured flow speeds exceeding 1 mm/s, whereas the experiments described above often involved faster flows with $Da_I \gg 1$. Higher flow speeds increase the effects of local Lagrangian stretching, which can either enhance or inhibit reaction for nonlinear reactions, depending on the rate of stretching,²⁰ causing reacted regions to grow or shrink. The Eikonal approximation of constant chemical speed assumes a lack of strain across the front, which is not true in the presence of strong stretching,⁹ and so, stretching may cause front speed to vary.

VII. SUMMARY AND FUTURE WORK

We have presented a new algorithm for measuring the chemical velocity and total velocity of reaction fronts in ARD systems, expanding our previous algorithm measuring front velocity and thickness in stagnant reaction-diffusion systems. The algorithm requires knowledge of the underlying fluid flow. We first validated the algorithm by tracking fronts in ARD simulations with uniform flow and simple enough initial conditions that we had clear *a priori* expectations for the front velocity. We further validated the algorithm by tracking simulated fronts approaching a burning invariant manifold (BIM) in a hyperbolic flow region. We also tracked fronts in experiments, using three different laboratory devices to show that the algorithm is self-consistent and that errors due to spatial discretization are negligible. We found experimental front tracking to be insensitive to user parameter choices. Finally, we showed one example of the sort of investigation enabled by front tracking, which makes a large number of local measurements of front velocity, throughout space and time. In a series of experiments in small-scale vortex flow and large-scale vortex flow, we observed that the distribution of chemical speeds varied

monotonically with flow speed: faster flow caused more regions with high chemical speed. Comparing experiments from the two different devices, we were surprised to find that plots of root-mean-square chemical speed varying with root-mean-square flow speed collapsed onto the same curve. The cause of the observed variation of chemical speed with flow speed remains an open question, worthy of future study.

Front tracking is applicable to either experimental measurements or simulation results, in steady or unsteady flows. The algorithm is independent of the size and speed of the ARD system since the calculations are done in camera units before being converted to physical units. This algorithm can accommodate situations where flow cannot be removed, such as ocean flows or combustion. This method also makes local measurements, providing far more information than most previous methods, which measured the asymptotic, global front speed in steady flows.^{11,15,18}

The algorithm allows testing new hypotheses about ARD dynamics. First, the local measurement of front speed could show whether fronts in experiments slow as they approach BIMs or bLCS, as they do in the simulation we used for validating the algorithm. Second, other barriers to front propagation may also be possible, and front tracking could locate them. For example, recent studies^{20,21} have found that excitable reactions are promoted mostly in regions where the Lagrangian stretching falls in an optimal range. Outside this range, fronts propagate slowly, or are driven to extinction by a process analogous to blowing out a flame. Measuring front speed might help determine whether blow-out causes well-defined barriers to reactive mixing. Third, our results in Sec. VI indicate that the constant front speed assumption, frequently used in BIM theory,²² may not always be accurate. Front tracking might quantify the parameter range over which the assumption is accurate. Fourth, front tracking also opens up opportunities to test the dynamic causes of frozen front phase transitions observed in open flows.^{10–12} Finally, other authors have recently speculated that front speed may depend on the front thickness,¹² a hypothesis that can be tested directly with our front tracking algorithm.

The algorithm can also have important practical applications. We have considered only the BZ reaction, but future measurements of chemical speed and its variation with flow speed in other chemical systems could reveal interesting and useful chemical kinetics. Industrial reactors are intended to maximize the overall reaction rate while minimizing the energy required by the mixers that drive flow. By locating regions of maximum front speed, front tracking could lead to improved reactor design. Ocean phytoplankton blooms occur at length scales inaccessible in the laboratory and depend on many complex factors, including ocean currents, temperature, nutrient availability, and plankton species. Determining phytoplankton front speed and its dependence on those factors might allow improved forecasting and control of phytoplankton blooms. Also, the variation of front speed might account for the genetic diversity of phytoplankton.⁴¹ Applying front tracking to combustion might reveal how different flames respond to wind, whether a flame reaches all

the fuel, what chemical mixes make the fastest flames, and which parts of flames grow fastest.

The algorithm leaves opportunity for future improvement as well. For example, we have implemented it only for two-dimensional domains, but the algorithm could generalize directly to three dimensions. Higher order time-stepping may also be possible. It would be especially helpful to account for the continuous change in the orientation of front elements. These further generalizations of front tracking could increase its usefulness and allow front tracking to provide insight into the growth dynamics of a multitude of systems.

ACKNOWLEDGMENTS

The authors are grateful for insightful conversations with N. T. Ouellette and J. G. Puckett and experimental design help from R. S. Russell and J. Tithof. We thank J. Wang for the results shown in Fig. 6(d). T. D. Nevins was supported by the Department of Defense (DoD) through the National Defense Science and Engineering Graduate Fellowship (NDSEG) Program.

¹M. A. Finney, *For. Ecol. Manage.* **211**, 97 (2005).

²B. Coriton, J. H. Frank, and A. Gomez, *Combust. Flame* **160**, 2442 (2013).

³K. S. Elvira, X. C. I. Solvas, R. C. R. Wootton, and A. J. deMello, *Nat. Chem.* **5**, 905 (2013).

⁴C. P. Schlick, P. B. Umbanhowar, J. M. Ottino, and R. M. Lueptow, *Chaos* **24**, 013109 (2014).

⁵A. W. Nienow, M. F. Edwards, and N. Harnby, *Mixing in the Process Industries* (Butterworth-Heinemann, 1997).

⁶A. P. Martin, *Prog. Oceanogr.* **57**, 125 (2003).

⁷T. D. Nevins and D. H. Kelley, *Chaos* **27**, 043105 (2017).

⁸R. A. Fisher, *Ann. Eugen.* **7**, 355 (1937).

⁹R. S. Spangler and B. F. Edwards, *J. Chem. Phys.* **118**, 5911 (2003).

¹⁰S. Saha, S. Atis, D. Salin, and L. Talon, *Europhys. Lett.* **101**, 38003 (2013).

¹¹S. Atis, S. Saha, H. Auradou, D. Salin, and L. Talon, *Phys. Rev. Lett.* **110**, 148301 (2013).

¹²T. Chevalier, D. Salin, and L. Talon, *Phys. Rev. Fluids* **2**, 043302 (2017).

¹³T. Chevalier, A. K. Dubey, S. Atis, A. Rosso, D. Salin, and L. Talon, *Phys. Rev. E* **95**, 042210 (2017).

¹⁴J. R. Mahoney and K. A. Mitchell, *Chaos* **25**, 087404 (2015).

¹⁵M. E. Schwartz and T. H. Solomon, *Phys. Rev. Lett.* **100**, 028302 (2008).

¹⁶B. F. Edwards, *Phys. Rev. Lett.* **89**, 104501 (2002).

¹⁷B. F. Edwards, *Chaos* **16**, 043106 (2006).

¹⁸M. Leconte, J. Martin, N. Rakotomalala, and D. Salin, *Phys. Rev. Lett.* **90**, 128302 (2003).

¹⁹Z. Neufeld, C. López, E. Hernández-García, and O. Piro, *Phys. Rev. E* **66**, 066208 (2002).

²⁰T. D. Nevins and D. H. Kelley, *Phys. Rev. Lett.* **117**, 164502 (2016).

²¹J. Wang, J. Tithof, T. D. Nevins, R. O. Colón, and D. H. Kelley, *Chaos* **27**, 123109 (2017).

²²D. Bargteil and T. Solomon, *Chaos* **22**, 037103 (2012).

²³J. Mahoney, D. Bargteil, M. Kingsbury, K. Mitchell, and T. Solomon, *Europhys. Lett.* **98**, 44005 (2012).

²⁴K. A. Mitchell and J. R. Mahoney, *Chaos* **22**, 037104 (2012).

²⁵J. R. Mahoney and K. A. Mitchell, *Chaos* **23**, 043106 (2013).

²⁶J. R. Mahoney, J. Li, C. Boyer, T. Solomon, and K. A. Mitchell, *Phys. Rev. E* **92**, 063005 (2015).

²⁷S. Gowen and T. Solomon, *Chaos* **25**, 087403 (2015).

²⁸P. Foerster, S. C. Muller, and B. Hess, *Science* **241**, 685 (1988).

²⁹J. Glimm, J. W. Grove, X. L. Li, K.-M. Shyue, Y. Zeng, and Q. Zhang, *SIAM J. Sci. Comput.* **19**, 703 (1998).

³⁰I.-L. Chern, J. Glimm, O. McBryan, B. Plohr, and S. Yaniv, *J. Comput. Phys.* **62**, 83 (1986).

³¹M. J. Ablowitz and A. Zeppetella, *Bull. Math. Biol.* **41**, 835 (1979).

³²V. K. Vanag and I. R. Epstein, *J. Chem. Phys.* **117**, 8508 (2002).

³³P. W. Megson, M. L. Najarian, K. E. Lilienthal, and T. H. Solomon, *Phys. Fluids* **27**, 023601 (2015).

³⁴See <http://www.me.rochester.edu/projects/dhkelleylab/> to download a Matlab script that performs the front tracking algorithm.

³⁵S. K. Scott, *Oscillations, Waves, and Chaos in Chemical Kinetics* (Oxford University Press Inc., New York, 1994).

³⁶P. M. Wood and J. Ross, *J. Chem. Phys.* **82**, 1924 (1985).

³⁷A. N. Zaikin and A. M. Zhabotinsky, *Nature* **225**, 535 (1970).

³⁸I. R. Epstein, *Chem. Eng. News Arch.* **65**, 24 (1987).

³⁹N. T. Ouellette, H. Xu, and E. Bodenschatz, *Exp. Fluids* **40**, 301 (2006).

⁴⁰T. H. Solomon and I. Mezic, *Nature* **425**, 376 (2003).

⁴¹F. d'Ovidio, S. De Monte, S. Alvain, Y. Dandonneau, and M. Lévy, *Proc. Natl. Acad. Sci. U.S.A.* **107**, 18366 (2010).